Template-Based B_1 Inhomogeneity Correction in 3T MRI Brain Studies

Marcelo A. Castro*, Jianhua Yao, Yuxi Pang, Christabel Lee, Eva Baker, John Butman, Iordanis E. Evangelou, and David Thomasson

***Abstract*—Low noise, high resolution, fast and accurate T_1 maps from MRI images of the brain can be performed using a dual flip angle method. However, B_1 field inhomogeneity, which is particularly problematic at high field strengths (e.g., 3T), limits the ability of the scanner to deliver the prescribed flip angle, introducing errors into the T_1 maps that limit the accuracy of quantitative analyses based on those maps. A dual repetition time method was used for acquiring a B_1 map to correct that inhomogeneity. Additional inaccuracies due to misregistration of the acquired T_1-weighted images were corrected by rigid registration, and the effects of misalignment on the T_1 maps were compared to those of B_1 inhomogeneity in 19 normal subjects. However, since B_1 map acquisition takes up precious scanning time and most retrospective studies do not have B_1 map, we designed a template-based correction strategy. B_1 maps from different subjects were aligned using a twelve-parameter affine registration. Recomputed T_1 maps showed an important improvement with respect to the noncorrected maps: histograms of all corrected maps exhibited two peaks corresponding to white and gray matter tissues, while unimodal histograms were observed in all uncorrected maps because of the inhomogeneity. A method to detect the best nonsubject-specific B_1 correction based on a set of features was designed. The optimum set of weighting factors for those features was computed. The best available B_1 correction was detected in almost all subjects while corrections comparable to the T_1 map corrected using the B_1 map from the same subject were detected in the others.**

***Index Terms*—B_1 inhomogeneity, brain, image registration, magnetic resonance images (MRI), T_1 mapping.**

Manuscript received July 10, 2009; revised May 26, 2010; accepted June 07, 2010. Date of publication June 21, 2010; date of current version November 03, 2010. The work of M. A. Castro was supported in part by CONICET (Argentina). *Asterisk indicates corresponding author*.

M. A. Castro is with the National Institutes of Health, Department of Radiology and Imaging Sciences (NIH-DR&IS), Bethesda, MD 20892 USA and also with CONICET, Universidad Tecnológica Nacional, Grupo de Investigación y Desarrollo en Bioingeniería (GIBIO), CP 1179 Buenos Aires, Argentina (e-mail: castroma@cc.nih.gov).

J. Yao, E. Baker, J. Butman, I. Evangelou, and D. Thomasson are with the National Institutes of Health, Department of Radiology and Imaging Sciences (NIH-DR&IS), Bethesda, MD 20892 USA (e-mail: jyao@cc.nih.gov; bakere@cc.nih.gov; jbutmana@cc.nih.gov; evangelouI@ninds.nih.gov; dthomasson@cc.nih.gov).

Y. Pang is with the National Institutes of Health, Department of Radiology and Imaging Sciences (NIH-DR&IS), Bethesda, MD 20892 USA and is also with Philips Healthcare, Cleveland, OH 44102 USA (e-mail: pangyu@mail.nih.gov).

C. Lee was with National Institutes of Health, Department of Radiology and Imaging Sciences (NIH-DR&IS), Bethesda, MD 20892 USA. She is now with the Department of Radiology, Georgetown University Medical Center, Washington DC 20007 USA (e-mail: leechrist@cc.nih.gov).

Color versions of one or more of the figures in this paper are available online at http://ieeexplore.ieee.org.

Digital Object Identifier 10.1109/TMI.2010.2053552

I. Introduction

ACCURATE estimation of T_1 relaxation time from magnetic resonance images (MRI) is essential for some clinical applications, such as dynamic contrast-enhanced MRI studies of cancer, which require low noise and high resolution over a large volume [1]–[3]. The variable flip angle method, which has been widely accepted to achieve those requirements in a reasonable time frame, is based on acquiring spoiled gradient recalled-echo (SPGR) images with various different flip angles with the repetition time (T_R) held constant. Despite longer acquisition times, multiple flip angles (from three up to ten) are preferred when imaging over a large T_1 range [4], [5]. However, according to Wang *et al.* for any given T_R/T_1 ratio, there exist two optimal flip angles that minimize the uncertainty in the estimated T_1 values [6].

Intensity inhomogeneity is often seen in MR images and is caused by many factors. However, the electromagnetic interaction with the object is the primary cause of that inhomogeneity [7]. Proper T_1 estimation requires minimizing the effects of spatial variations of the transmitted flip angle α_T at every voxel, which is related to the prescribed flip angle α as $\alpha_T = \alpha K(x, y, z)$, where K denotes the spatial variation of the radiofrequency (RF) or B_1 field [4]. In MRI systems with low static magnetic field B_0, $(< 0.5\ T)$ the Larmor frequency (i.e., the precession frequency of the hydrogen nuclei around the direction of the applied magnetic field), and hence the frequency of the B_1 field, is very low. In that case, since the dimension of the human body is a small fraction of that wavelength, its interaction with the B_1 field can be neglected. However, the main limitation of low B_0 field systems is their low signal-to-noise ratio (SNR), which is proportional to the field strength B_0 [8]. Therefore, higher fields (e.g., 3T) are preferred to increase SNR. However, B_1 inhomogeneity also increases because the influence of wavelength becomes much more relevant at 3T [9]. The wavelength in tissue, which is proportional to the inverse of the square root of the dielectric constant, is reduced due to higher dielectric constant in biological tissue (typically between 10 and 100). If the wavelength of the RF field is of the same order as the imaged object then either destructive or constructive interferences of the transmitted RF field may be observed resulting in a regional signal loss or regional brightening, respectively [10].

A discussion about different techniques used to address this problem has been presented in detail in at least three major reviews [11]–[13]. According to those reviews, correction methods can be classified in two main groups: retrospective

methods and prospective methods. The retrospective methods solve the undetermined problem (1) using only the uncorrected images under different assumptions about the acquisition process. The original and corrected intensities are related by

$$v(x,y,z) = u(x,y,z).b(x,y,z) + N(x,y,z) \qquad (1)$$

where u is the true intensity spatial distribution, v is the measured voxel intensity, b is the bias or inhomogeneity field and N is the additive noise distribution at a voxel location $x = (x,y,z)$. On the other hand, prospective methods rely on the acquisition of additional data or *prior knowledge* resulting in a subject-specific correction. The aim of both approaches is to improve image quality to make quantitative analyses reliable.

A large number of retrospective methods to correct B_1 inhomogeneity can be found in the literature [13]–[27] and can be grouped in at least three major categories. There is a first category known as surface fitting that relies on the assumption that the inhomogeneity field is slowly varying. Therefore, it can be approximated by a parametric smooth function whose parameters can be estimated either by segmenting a set of voxels throughout different tissues [15], [17], [24], which provides information about the inhomogeneity map, or by entropy minimization [18], [19], [22].

A second category includes methods that exploit the slowly varying characteristic of the inhomogeneous field to separate it from the true image by lowpass filtering. Due to their simplicity and efficiency they have been widely used [13], [14], [21]. Recently, lowpass filtering methods have been extended using the wavelet transform and were shown to be effective in removing inhomogeneity in images acquired with different kind of coils [16], [20].

There is a third group of retrospective methods known as statistical methods that assume that the inhomogeneity field follows a given distribution, or model that inhomogeneity as a random process [23], [27].

A particular approach proposed by Sled *et al.* is the N3 method [25], which derives a nonparametric model of the tissue intensity directly from the data, avoiding in this way some of the restrictive model assumptions found in other similar methods. Particularly, the N3 method does not require a model of the tissue intensities in terms of discrete tissue classes, nor does it rely on a segmentation of the volume into homogeneous regions. The optimization criterion is to find the smooth, slowly varying multiplicative field that maximizes the frequency content of the distribution of tissue intensities. Like in most other retrospective nonuniformity correction methods, if the object is itself a smooth and slowly varying field then the correction field that maximizes that frequency content will also remove the natural variations of the object. Particularly, the underlying cell structure of different regions of the brain induces a range of intensities in structural T_1-weighted (T_1w) MRI scans. An example is that of subcortical tissues in regions of the thalamus and lenticular nucleus, whose intensity in T_1w MRI is between that of pure white matter (WM) and gray matter (GM) and can exhibit a spatially varying range of intensities. Studholme developed a correction of brain MRI image distortion to address this limitation [26]. They performed a manual segmentation-based bias estimation to provide an accurate tissue intensity template for bias correction and a 3-D model of the intensity variation across the brain is created by fitting a *B*-spline model to this intensity profile. The aim of this method is to capture the local intensity variation within a given kind of tissue, which should not be removed when compensating the global inhomogeneity due to the acquisition process, and use it as a reference template. MRI data was registered to the target reference template using a free form volume deformation procedure to separate smoothly varying inhomogeneity effects from underlying anatomical structure.

Different prospective methods to compensate B_1 field inhomogeneity by acquiring additional images have been presented in the past. Ishimori *et al.* proposed a method to estimate and correct B_1 inhomogeneity that uses multiple SPGR for 3T spin-echo MRI, which relied on the acquisition of several images with different echo times (T_E) and flip angles for a fixed T_R [28]. To compute B_1 corrected T_1 maps, Mihara *et al.* used multisliced spoiled gradient echo sequences on a 1.5T scanner with different T_R and flip angles, requiring 29 min to acquire the three images for each brain [29]. Treier presented a combined T_1 and B_1 mapping technique for T_1 estimation in abdominal contrast-enhanced MRI [30] that computes T_1 maps from two T_1w images acquired using two optimal flip angles [6] and compensates the B_1 inhomogeneity using a subject-specific B_1 map acquired by means of a dual T_R method [31]. Deoni presented a method that combines the usual multiangle SPGR data with at least one inversion-prepared SPGR data in order to obtain an unique solution for the T_1 map, the factor proportional to the longitudinal magnetization and the spatial variation of the radiofrequency field by least square minimization, which requires 10 min for 1 mm^3 isotropic T_1 and B_1 maps acquisition [32] with less than 5% of error, and 6:40 min for a T_1 map ($128 \times 128 \times 160$ matrix).

In the clinical setting, it is beneficial to minimize scanning time and it would be desirable that B_1 corrections may be made from a template, obviating the need for obtaining a B_1 map each and every time a patient is scanned. Using template B_1 maps would also allow more accurate quantitative analyses in studies where B_1 maps were not previously acquired. However, using a single template B_1 map for all corrections may introduce additional inaccuracies. Alternatively, a set of template B_1 maps might minimize those inaccuracies provided that an efficient method to detect the most realistic B_1 map based on a set of features is available.

Our template-based B_1 correction method is based on Treier's technique but with the incorporation of modules to align acquired images and to transform B_1 maps from other subjects. We validated the methodology using phantoms and investigated the shift in the mean value of the corrected T_1 map when compared to the noncorrected one (T_1^{nc}) also reported by Treier [30]. T_1w images used to produce T_1 maps must be aligned. We incorporated an image registration step and compared the effects of misalignment between both acquired T_1w images to those of B_1 inhomogeneity on the computed T_1 maps. A sample of 19 normal volunteers who underwent brain MRI scanning was considered for this study. White and gray matter relaxation times were estimated from corrected maps

and compared to previously reported data [32]. Preliminary results have already been presented [33]. B_1 inhomogeneity in T_1 maps computed from registered images was also compensated using B_1 maps acquired from other subjects. Those maps were previously aligned using an affine registration algorithm. The performance of those corrections was evaluated. An automatic method to detect the B_1 map that performs the best correction when compared to the map corrected with the proper B_1 map (called reference map, T_1^{ref}) was designed based on a set of features and evaluated.

II. Methods

A methodology to obtain T_1 maps from MRI images of the brain with two optimal flip angles was used in nineteen normal volunteers. In order to reduce the inhomogeneity produced by the fluctuation around the prescribed flip angle, which is particularly problematic in high field MRI studies, B_1 maps were generated using a dual T_R strategy [31] and incorporated into the T_1 calculation. The implementation of the B_1 correction methodology was evaluated using a phantom and the results were compared to those using an inversion recovery technique and the retrospective N3 method. Effects of image misalignment on the quality of T_1 maps were investigated by rigidly registering the two 3-D T_1w images acquired with different flip angles and compared to those due to B_1 inhomogeneity. A Brain Extraction Tool (BET), which is a 3-D method that uses a deformable model that evolves to fit the brain surface by the application of a set of locally adapted forces [34], was used to extract the brains from the T_1 maps in order to compute intensity histograms. In those histograms, each tissue type, e.g., WM, GM, and cerebrospinal fluid (CSF), was modeled by Gaussian functions. In order to estimate the peak T_1 value and its standard deviation for WM and GM tissues, mixed classes were neglected and a three-Gaussian fitting was used [35]. Ideal histograms of the whole brain should exhibit two peaks corresponding to the WM and GM tissues, while CSF does not contribute to a third peak due to its small volume. In addition, each T_1 map from aligned images was corrected using the B_1 maps from all the other subjects. For that purpose, high flip angle T_1w images from different subjects were registered to each other using a twelve-parameter affine registration with mutual information metric and linear interpolation, and the transformation obtained was applied to the B_1 maps. The influence of the object position on the B_1 maps was studied. T_1 maps corrected using both the proper B_1 map and the transformed B_1 maps from other subjects were compared and the percentage of voxels whose relative difference was less than a given threshold was used to quantify the quality of the correction. The whole sample was divided into two sets. From the reference set several features were computed and used to characterize the quality of the corrections in each subject in the learning set, which was utilized to detect the best possible correction. A training procedure was performed to find the optimum set of weighting factors for each feature.

A. Subjects and Imaging

Nineteen normal volunteers (9 males and 10 females) with ages between 23 and 62 (mean $\pm$ stdev $=$ 39.1 ± 11.3) without history of neurological diseases were considered in this study. The imaging protocol was approved by the institutional review board and informed consent was obtained from all subjects. Imaging was performed using a 3T Philips system (Philips, Best, The Netherlands) equipped with Explorer gradients using a SENSE head coil. Two 3-D T_1w fast field echo (FFE) images (48 slices, FOV $=$ 240 mm $\times$ 240 mm, slice thickness $=$ 3.0 mm, matrix $=$ 480×480) in an axial orientation were acquired using a dual flip angle SPGR protocol ($T_R/T_E/FA_1/FA_2$ $=$ 6 ms/2.3 ms/5°/15°), with flip angles selected to achieve maximum accuracy in the range of white and gray matter tissue [30]. Another two T_1w images (24 slices, FOV $=$ 240 mm $\times$ 240 mm, slice thickness$=$ 6.0 mm, matrix$=$ 240×240) were simultaneously collected to produce B_1 maps from a dual-T_R SPGR protocol ($T_{R1}/T_{R2}/FA/T_E = 50$ ms/250 ms/60°/5 ms). The reduced resolution was chosen to avoid increased acquisition times. Repetition times were chosen based on the optimum ratio in the range of 4-6 in order for the ratio between signal intensities from both images to be sensitive to flip angle variations, under the condition $T_{R1} < T_{R2} < T_1$[31]. The total acquisition time for the four images and B_1 map generation is 7:30 min.

B. Misalignment Correction

A 3-D rigid registration algorithm based on the mutual information metric presented by Mattes *et al.* [36] using linear interpolation was incorporated into our code in order to correct any possible misalignment between the two T_1w images used for the T_1 map calculation. The other two T_1w images used for the B_1 maps are not registered since they are simultaneously acquired. The mutual information metric (MI) is an image discrepancy measure based on the analysis of the histograms of both the reference and test images (2). Cost function minimization requires the computation of the joint probability distributions (p) as well as the marginal probability distributions of both the reference (p_R) and test images (p_T). The six parameters of the transformation are obtained from such minimization. The rigid transformation is suitable for the expected movement of the head during the scanning and the mutual information metric is a fast and accurate way to estimate the image discrepancy given the small misalignments expected in this kind of studies

$$MI = -\sum_{l}\sum_{k} p\left(l,k \mid \mu\right)\frac{p\left(l,k \mid \mu\right)}{p_T\left(l \mid \mu\right)p_R\left(k\right)}. \qquad (2)$$

C. T_1 Calculation With Correction of B_1 Inhomogeneity

The variable flip angle method for T_1 estimation is based on the consecutive acquisition of T_1w SPGR (T_1-FFE) sequences with different flip angles. Our implementation of the T_1 map generation is based on the two optimal flip angles method [6], which is described in the following paragraphs. Each acquired T_1w image has a theoretical signal intensity S that depends on the prescribed flip angle α, the longitudinal magnetization M_0, the echo time T_E, the repetition time T_R, and the relaxation times T_1 and T_2 (3). That theoretical signal intensity can

also be expressed as a linear relation between $S/\sin(\alpha)$ and $S/\tan(\alpha)$ (4)

$$S = M_0 \frac{\sin(\alpha)\left(1 - e^{-T_R/T_1}\right) e^{-T_E/T_2}}{1 - e^{-T_R/T_1}\cos(\alpha)} \quad (3)$$

$$\left(\frac{S}{\sin(\alpha)}\right) = e^{-T_R/T_1}\left(\frac{S}{\tan(\alpha)}\right) + M_0\left(1 - e^{-T_R/T_1}\right) e^{-T_E/T_2}. \quad (4)$$

The factor $\exp(-T_E/T_2)$ in (3) and (4) is approximately 1 since the echo time in our T_1w images ($T_E = 2.3$ ms) is much smaller than the expected T_2 value for white and gray matter at 3T, which ranges between 50 ms and 100 ms [30], [37]. Under this assumption the two optimal prescribed flip angles can be computed from (5), resulting in $\alpha_1 = 5°$ and $\alpha_2 = 15°$ in order for the T_1 estimation to be accurate in the range for typical white and gray matter values at 3T [32]. The T_1 precision in (5) is maximized for $f = S_1/S_E = S_2/S_E = 0.71$ when fitting a polynomial for each T_R/T_1 ratio over a wide range [32], [37], where $E_1 = \exp(-T_R/T_1)$, S_1 and S_2 are the signal intensities of two given T_1w images I_1 and I_2, and S_E is the Ernst signal

$$\alpha = \arccos\left[\frac{f^2 E_1 \pm \left(1 - E_1^2\right)\sqrt{1 - f^2}}{1 - E_1^2\left(1 - f^2\right)}\right]. \quad (5)$$

For those signal intensities S_1 and S_2 corresponding to flip angles α_1 and α_2, the slope m in the linear relation (4) can be obtained (6) and used to compute T_1 (7) at every image voxel

$$m = \frac{\frac{S_1}{\sin(\alpha_1)} - \frac{S_2}{\sin(\alpha_2)}}{\frac{S_1}{\tan(\alpha_1)} - \frac{S_2}{\tan(\alpha_2)}} \quad (6)$$

$$T_1 = -\frac{T_R}{\ln(m)}. \quad (7)$$

B_1 inhomogeneity maps are generated from a dual T_R technique where two images are acquired with different T_R but the same T_E and prescribed flip angle. Equation (8) shows the ratio r of the image intensities after applying the first-order approximation to the exponential terms. Therefore, B_1 inhomogeneity values are computed from the ratio between the transmitted and prescribed flip angles (9) [31]

$$r = \frac{1 + n\cos(\alpha_T)}{n + \cos(\alpha_T)} \quad (8)$$

$$B_1 = \frac{1}{\alpha}\arccos\left[\frac{rn - 1}{n - r}\right] \quad (9)$$

where n is the ratio between the smaller and the larger repetition times ($n = 5$ for our acquisitions, as it was discussed in Section II-A). Maps are tri-linearly interpolated to obtain B_1 inhomogeneity values at I_1 and I_2 image nodes. Since B_1 maps provide a distribution of correction factors for the ideally uniform prescribed flip angle, the corrected slope m_{corr}(10) is used to compute the corrected T_1 values at every voxel [30], which is given by (11)

$$m_{\text{corr}} = \frac{\frac{S_1}{\sin(B_1\alpha_1)} - \frac{S_2}{\sin(B_1\alpha_2)}}{\frac{S_1}{\tan(B_1\alpha_1)} - \frac{S_2}{\tan(B_1\alpha_2)}} \quad (10)$$

$$T_1^{\text{corr}} = -\frac{T_R}{\ln(m_{\text{corr}})}. \quad (11)$$

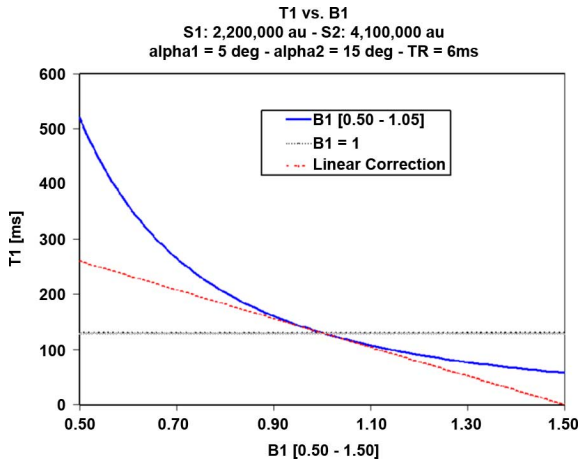

Fig. 1. T_1 value computed for typical maximum intensities S_1 and S_2 in our brain MRI acquisitions at flip angles of 5° and 15°, and $T_R = 6$ ms with: no B_1 correction (textured line), B_1 correction (solid line), linearized B_1 correction (dotted line). S_1 and S_2 do not necessarily correspond to any real tissue.

In order to properly compute the T_1 maps from the T_1w images, both with and without B_1 correction, those images are previously aligned using six-parameter rigid registration with a mutual information metric and linear interpolation, using 64 histogram bins and the number of spatial samples equal to 1% of the image pixels.

Fig. 1 shows the relation between the corrected T_1 values and the B_1 correction factor for a typical set of signal intensities, flip angles and repetition time computed using (7) and (11). It can be observed that only if the B_1 inhomogeneity correction factors of those voxels in the volume are symmetrically distributed around $B_1 = 1.0$ and the relation between B_1 and the corrected T_1 value is linear, then it is expected to have a corrected T_1 map that preserves the mean value with respect to the uncorrected one. But in real cases none of those assumptions can be observed. B_1 inhomogeneity correction factors do not necessarily have a mean value of 1.0, therefore, there is no physical reason to expect a symmetrical distribution. In addition, their dispersion is large enough to have a considerable amount of voxels away from the region where the linear approximation is acceptable. If the distribution of correction factors were symmetrically centered at $B_1 = 1.0$, corrected T_1 map will still have a higher mean value than that of the uncorrected one because of the nonlinear relation (Fig. 1).

It is assumed that the T_1w images for a particular subject are aligned with the corresponding B_1 map. However, even if small misalignments were present, their impact is expected to be small due to the small displacements expected in this kind of studies and the typical smoothness of B_1 maps. In order to estimate the typical maximum error because of those possible misalignments the signal intensities S_1 and S_2 at a voxel where the B_1 map exhibits the maximum variation in a selected subject were used to compute the corrected T_1 value without misalignment and with a displacement of 5 mm between the T_1w images and the B_1 map. That maximum error in the T_1 estimation was 4%, which was much smaller than the error between the B_1-corrected and uncorrected T_1 maps (14%). Most voxels will exhibit much smaller errors ($< 4\%$) given the smoother variations in the B_1 map.

D. N3 Method

The prospective B_1 inhomogeneity correction method described in the previous section was compared to the retrospective N3 method [25] to evaluate the effect of the lack of information in retrospective methods when compared to prospective methods. The MIPAV implementation was used for comparison purposes.[1] The N3 method is an automatic nonparametric method for MRI inhomogeneity image correction that assumes a model of image formation as described in (1). Consider a noise-free case where the true intensities u at each voxel location $\boldsymbol{x} = (x, y, z)$ are independent identically distributed variables. In that case, the logarithm of those variables are related by

$$v_L(x,y,z) = u_L(x,y,z) + b_L(x,y,z) \tag{12}$$

where v_L, u_L, and b_L denotes $\log(v)$, $\log(u)$ and $\log(b)$, respectively. The distribution of values that each of these variables take over the considered volume can be regarded as the probability distribution of random variables, whose probability densities will be called V_L, U_L and B_L, respectively. Under the assumption that u_L and b_L are independent random variables, the distribution of their sum is found by convolution

$$\begin{aligned} V_L(v_L) &= B_L(b_L) * U_L(u_L) \\ &= \int B(u_L - b_L)\, U(b_L)\, db_L. \end{aligned} \tag{13}$$

Therefore, the nonuniformity distribution B can be viewed as blurring the intensity distribution U, which reduces its high frequency components. The aim of this method is to find the smooth, slowly varying, multiplicative field that maximizes the frequency content of U. A distribution U is proposed by sharpening the distribution V, and then a smooth field that produces a distribution U close to the one proposed is estimated. The distribution B is typically well approximated by a unimodal distribution. The noise-free assumption makes B approximately Gaussian. Since any Gaussian distribution can be decomposed into a convolution of narrower Gaussian distributions the space of all U distributions corresponding to Gaussian distributed B can be searched incrementally by deconvolving narrow Gaussian distributions from subsequent estimates of U iteratively.

The T_1 maps using B_1 correction (T_1^{ref}), N3 correction (T_1^{N3}) and no correction (T_1^{nc}) in a set brain MRI images of normal volunteers were compared. The percentage of voxels in T_1^{N3} and T_1^{nc} whose relative difference is less than 10% when compared to T_1^{ref} is computed for that purpose.

E. Template Based B_1 Correction

In order to reduce the scan time and also to correct studies with no previous B_1 map, we designed a template based correction strategy. This strategy corrects B_1 inhomogeneity in a given subject by using a B_1 map from another subject after proper registration.

In this method, we first build a library of B_1 maps from training studies acquired by the dual -T_R method. Then, given a new study i, we examine it against every study j in the library (we call it a template). The examination is conducted as follows. First, the T_1w images from study i and template j are aligned by means of a twelve-parameter affine registration method with mutual information metric and linear interpolation, using 64 histogram bins and the number of spatial samples equal to 1% of the image pixels.

Afterwards, the B_1 map of template j is aligned according to that transformation in order to match the geometry of the subject under study i. The B_1 correction of study i is performed in the same way as described in the Section II-C. Small inaccuracies in the registration due to the use of the affine registration are expected to have a small effect on the corrected T_1 maps because of the typical smoothness of the B_1 maps (see Section II-C). To clarify the method, we define the following.

$T_{1\,(i)}^{nc}$	T_1 map of study i before correction.
$T_{1\,(j)}^{nc}$	T_1 map of template j before correction.
$B_1^{(i)}$	B_1 map of study i (dual T_R method), if exists.
$B_1^{(j)}$	B_1 map of template j (dual T_R method).
$T_{1\,(i)}^{i} = T_{1\,(i)}^{\text{ref}}$	Corrected T_1 map of study i using $B_1^{(i)}$, if exists.
$T_{1\,(i)}^{j}$	Corrected T_1 map of study i using $B_1^{(j)}$.

For each template correction j of a study i a total of six features are extracted from $T_{1\,(i)}^{nc}$, $T_{1\,(j)}^{nc}$, and $T_{1\,(i)}^{(j)}$ and compared to their reference values. A metric function M comparing the features computed for a given correction $j(F_{m\,(i)}^{(j)})$ and the reference values F_m^{ref}, is designed to select the most suitable B_1 map for study i from the library. Each feature m contributes with a given weighting factor $w^{(m)}$. The meaning of each feature and the training process to determine the optimum set of weighting factors is described in Section II-F. The template selection processing for study i can be written as described in (14), where t is the selected template for study i. For clarity, we define $T_{1\,(i)}^{\text{tem}}$ as the T_1 map corrected by our template based method. We also define T_1^{nc}, $T_1^{(j)}$, T_1^{tem}, T_1^{ref} to represent $T_{1\,(i)}^{nc}$, $T_{1\,(i)}^{(j)}$, $T_{1\,(i)}^{\text{tem}}$, $T_{1\,(i)}^{\text{ref}}$, for a known study i. Fig. 2 exemplifies the methodology

$$\begin{aligned} t = \arg\min_j \left(M\left(F_{m\,(i)}^{(j)}, F_m^{\text{ref}}\right)\right), \text{ with } M\left(F_{m\,(i)}^{(j)}, F_m^{\text{ref}}\right) \\ = \frac{\sum_{m=1}^{N_{\text{feat}}} w^{(m)} \left| F_{m\,(i)}^{(j)} - F_m^{\text{ref}} \right|}{N_{\text{feat}}}. \end{aligned} \tag{14}$$

F. Training and Metric Function Optimization

In the training procedure, both T_1w images and the B_1 map are available, and T_1^{ref} and T_1^{nc} are computed for all studies. Ten studies were randomly selected and assigned to a learning set (LS) in order to determine the optimum set of weighting factors ($N_{\text{LS}} = 10$). The remaining studies were assigned to a reference set and used to determine the reference value for each

[1] http://mipav.cit.nih.gov

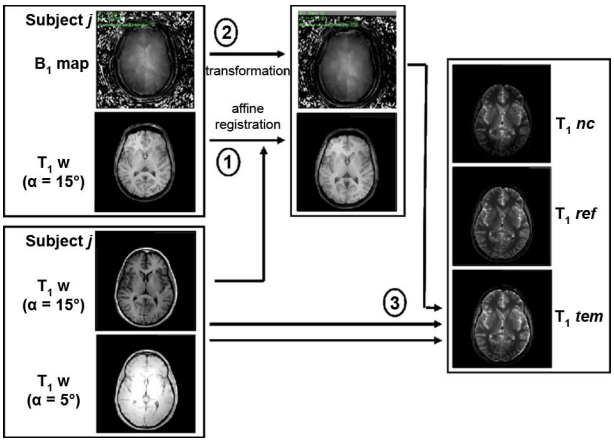

Fig. 2. Methodology to generate a B_1-corrected T_1 map of subject i using the B_1 map from subject j. (1) High-flip-angle T_1w images of subjects i and j are aligned. (2) The transformation is applied to the B_1 map of Subject j. (3) T_1w images of Subject i along with the transformed B_1 map from Subject j are used to generated T_1^{tem}. If the B_1 map of Subject i is available, T_1^{ref} can be computed. If no B_1 map is used, the uncorrected T_1^{nc} map is generated.

feature (F_m^{ref}) needed to perform that optimization $(N_{\text{ref}} = 9)$. For each template correction j of every map i in LS $(T_{1\,(i)}^{(j)})$, the percentage of voxels having a difference less than 10% with respect to $T_{1\,(i)}^{\text{ref}}$ is computed and compared to the same percentage for $(T_{1\,(i)}^{nc})$. The ratio between those two percentages [for $T_{1\,(i)}^{\text{ref}}$ and $(T_{1\,(i)}^{nc})$] is computed and normalized between 0 (worst correction) and 1 (best correction), and a ranking list L_1 of all those ratios $(R_{(i)}^{(j)})$ is created. The correction j with the highest value $(R_{(i)}^{(j)} = 1)$ is considered the best correction available for the subject under study i, producing a map called $T_{1\,(i)}^{\text{opt}}$. Note that this characterization was used instead of the means square difference because it is less affected by large differences in regions where the methodology is not designed to work well. No difference in the ranking list was observed when using other thresholds different from 10%.

A set of six features with different weighting factors are considered to detect $T_{1\,(i)}^{\text{tem}}$ and a training process is performed to estimate the optimum set of factors so that $T_{1\,(i)}^{\text{tem}}$ equals $T_{1\,(i)}^{\text{opt}}$. Every feature m computed for every $T_{1\,(i)}^{(j)}$ in LS $(F_{m\,(i)}^{(j)})$ is compared to the corresponding reference value (F_m^{ref}). The absolute value of the difference between them $(D_{m\,(i)}^{(j)} = |F_{m\,(i)}^{(j)} - F_m^{TS}|)$ is computed, expecting lower values for better corrections (i.e., corrections that result in maps comparable to $T_{1\,(i)}^{\text{ref}}$). For a given feature m from subject i, $D_{m\,(i)}^{(j)}$ values are normalized between 0 and 1

$$F_2^{\text{ref}} = \frac{1}{N_{\text{ref}}} \sum_{i=1}^{N_{\text{ref}}} \sigma\left(T_{1\,(i)}^{\text{ref}}\right)$$

$$F_3^{\text{ref}} = \frac{1}{N_{\text{ref}}} \sum_{i=1}^{N_{\text{ref}}} T_{1\,(i)}^{\text{ref}}\Big|_{\text{WM}}$$

$$F_4^{\text{ref}} = \frac{1}{N_{\text{ref}}} \sum_{i=1}^{N_{\text{ref}}} T_{1\,(i)}^{\text{ref}}\Big|_{\text{GM}}. \tag{15}$$

TABLE I
LIST OF FEATURES COMPUTED OVER THE LEARNING SET. $V_{(i)}$ DENOTES THE BRAIN VOLUME IN T_1 MAP i, AND σ DENOTES THE DISPERSION OF THE NORMALIZED INTENSITY HISTOGRAM OF A GIVEN T_1 MAP

Description	Features for template correction *j* of T_1 map *i*
Comparison between the mean value of the uncorrected T_1 map ($T_1^{nc}{}_{(i)}$) and that of the subject whose B_1 map will be used for the correction ($T_1^{nc}{}_{(j)}$)	$F_{1\,(i)}^{(j)} = \left\| \frac{1}{V_{(j)}} \sum_{xyz} T_1^{nc}(j)(x,y,z) - \frac{1}{V_{(i)}} \sum_{xyz} T_1^{nc}(i)(x,y,z) \right\|$
Dispersion of the histogram of template correction map $T_1{}^{(j)}{}_{(i)}$	$F_{2\,(i)}^{(j)} = \sigma(T_{1\,(i)}^{(j)})$
WM peak in the histogram of template correction map $T_1{}^{(j)}{}_{(i)}$	$F_{3\,(i)}^{(j)} = T_1^{(j)}(i)\Big\|_{WM}$
GM peak in the histogram of template correction map $T_1{}^{(j)}{}_{(i)}$	$F_{4\,(i)}^{(j)} = T_1^{(j)}(i)\Big\|_{GM}$
Ratio between maximum values of WM and GM peaks in the 3-Gaussian curve fitted from normalized histogram of template correction map $T_1{}^{(j)}{}_{(i)}$	$F_{5\,(i)}^{(j)} = g(T_1^{(j)}{}_{(i)}\Big\|_{WM}) \,/\, g(T_1^{(j)}{}_{(i)}\Big\|_{GM})$
Ratio between the minimum of maximum values of WM and GM peaks and the value of the valley between peaks, in the 3-Gaussian curve fitted from normalized histogram of $T_1{}^{(j)}{}_{(i)}$	$F_{6\,(i)}^{(j)} = \min(g(T_1^{(j)}{}_{(i)}\Big\|_{WM}), g(T_1^{(j)}{}_{(i)}\Big\|_{GM})) \,/\, g(T_1^{(j)}{}_{(i)}\Big\|_{V}$

Following, a brief description of the meaning of those features is included (see Table I). $D_{1\,(i)}^{(j)}$ compares the mean values of the T_1 map to be corrected (i) and that of the uncorrected T_1 map whose B_1 map will be used for the correction (j). It is expected that a B_1 map from a subject with an uncorrected T_1 map whose mean value significantly differs from that of the T_1 map to be corrected, will not perform an acceptable correction. Given that the BET algorithm [34] may fail when extracting the brain from inhomogeneous images, the corrected T_1 map is used as a mask. $D_{2\,(i)}^{(j)}$ compares the dispersion of the histogram of a given template correction with the average dispersion computed over the reference set. $D_{3\,(i)}^{(j)}$ compares the T_1 value of the white matter (WM) peak in the histogram of a given template correction with the average T_1 value of the white matter peak computed over the reference set. $D_{4\,(i)}^{(j)}$ performs the same comparison as $D_{3\,(i)}^{(j)}$, but for the gray matter (GM) peak. $D_{5\,(i)}^{(j)}$ is used to find the template correction whose T_1 map has a histogram with the minimum ratio between the maximum values of the white matter and gray matter peaks in the three-Gaussian curve fitted from the normalized histogram $(g(T_{1(i)}^{(j)})|_{\text{WM}}$ and $g(T_{1(i)}^{(j)})|_{\text{GM}})$. $D_{6\,(i)}^{(j)}$ is used to find the correction whose T_1 map has a histogram with the minimum ratio between $\min(g(T_{1(i)}^{(j)})|_{\text{WM}}, g(T_{1(i)}^{(j)})|_{\text{GM}})$ and the value at valley between peaks $(g(T_{1(i)}^{(j)})|_V)$ in the three-Gaussian curve fitted from the normalized histogram. It was observed that lower values of these last two features (F_5 and F_6) are usually

associated to better corrections. Given the lack of information about what the reference values F_5^{ref} and F_6^{ref} should be, they were set to 0 in order to represent that the minimum will be searched. For feature F_1 the reference value is clearly 0, while for features F_2, F_3, and F_4, those reference values are computed as the averaged dispersion, WM and GM peaks of the histograms of reference maps (15). No correlation was found between the age, head size, and sex of a subject and the best available template. Therefore, they were not included as features.

For each subject i in LS and each correction j, a ranking list L_2 of the metric function M is created. The best correction $(j = t)$ detected by the method produces a corrected T_1 map $T_{1\,(i)}^{\text{tem}}$, as it was defined in Section II-E. Afterwards, the correction t is searched in the ranking list L_1, and the number $R_{(i)}^t$ is retrieved. If the method detects the best correction available, then $T_{1\,(i)}^{\text{tem}} = T_{1\,(i)}^{\text{opt}}$ and $R_{(i)}^t = 1$. In order to find the optimum set of weighting factors (w_{opt}) an optimization process is performed

$$w_{\text{opt}} = \arg\max_{w}(R(w))$$
$$R(w) = \frac{\sum_{i=1}^{N_{\text{LS}}} R_{(i)}^t(w)}{N_{\text{LS}}};\ w = (w_1, \ldots, wN_{\text{feat}}). \quad (16)$$

III. Results

A. Phantom Evaluation of the B_1 Correction Methodology

The performance of the B_1 correction methodology was evaluated by means of a spherical phantom filled with doped water. Fig. 3 shows the intensity distributions at a middle slice for both the noncorrected (a) and B_1 corrected (b) T_1 maps. Inhomogeneities observed near the phantom wall are due to B_0 effects in the T_1w images acquired to compute the B_1 map. The effect is propagated to the B_1 map and consequently to the corrected T_1 map, as shown in Fig. 3(b). These susceptibility artifacts appear at interfaces of substances with different susceptibilities, especially at higher field strengths since the magnetic susceptibility is proportional to the field strength B_0.

T_1 histograms for the whole phantom were generated for the non-corrected and B_1 corrected T_1 maps, as well as for the T_1 map computed from T_1w images whose inhomogeneity was previously corrected using the retrospective N3 method [see Fig. 3(c)]. The N3 method preserves the mean T_1 value (269 ms compared to 279 ms of the noncorrected map of the whole phantom), which strongly differ from the reference value obtained using an inversion recovery technique (365 ms). On the other hand, B_1 corrected map has a mean T_1 value of 327 ms, which is closer to that value. The length of the interval of relaxation times in the normalized histogram of the uncorrected map whose frequency is greater than 1% is 151 ms around its mean value, and 88% of the voxels fall in that interval. For the B_1 corrected map, that length drops to 137 ms and 92% of the voxels fall in that interval.

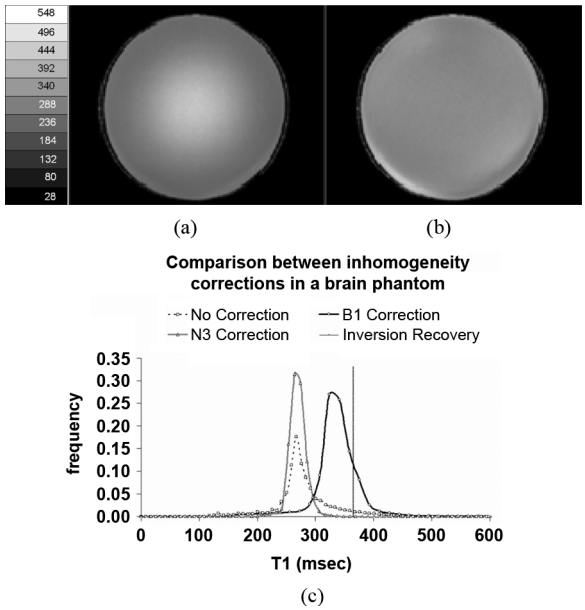

Fig. 3. Intensity distributions at a middle slice for both the noncorrected (a) and B_1 corrected (b) T_1 maps. Intensity histograms for the noncorrected, B_1 corrected and N3 corrected T_1 maps of the whole spherical phantom compared to the T_1 value measured with an inversion recovery technique (c).

B. Phantom Evaluation of the Effects of Object Positioning

B_1 maps depend on the location of the object within the scanner. Therefore, it is expected that B_1 maps of the same subject acquired at different locations and properly registered will perform different corrections. The proposed methodology might be affected if the template B_1 map was acquired at a different position from where the subject whose T_1 maps will be corrected was scanned. However, the displacements expected in routine brain scans of different subjects are small compared to the typical size of the heads. In order to estimate those displacements, the bounding box containing the brain at the middle slice was identified and the percentage of the pixels not covered by the bounding box at each side was recorded and averaged for the 19 subjects. Their values (mean $\pm$ stdev) were: a) right: $(17.6 \pm 1.1)\%$; b) left: $(17.7 \pm 1.5)\%$; c) anterior: $(12.4 \pm 3.0)\%$; d) posterior: $(4.7 \pm 2.4)\%$; e) inferior: $(30.2 \pm 3.1)\%$; f) superior: $(5.8 \pm 2.1)\%$. These observations show a consistency in the position of the heads in the scanner among subjects. The maximum displacement in the left–right direction at the middle slice was 0.58 cm, which was much smaller than the maximum distance in that direction (22 cm).

In order to estimate the error introduced by a typical displacement of an object within the scanner, a cylindrical phantom with doped water was imaged in two different positions: at the center of the scanner and 1.7 cm apart in a direction perpendicular to the axis. This distance is about three times the maximum displacement observed in routine brain scans. T_1w images for the T_1 map and B_1 map were acquired and the T_1 map was computed without B_1 correction (T_1^{nc}), corrected using the B_1 map acquired at the same position (T_1^{ref}) and corrected using the B_1 map acquired at a position 1.7 cm apart along the direction of the displacement perpendicular to the axis (T_1^{tem}), after registration.

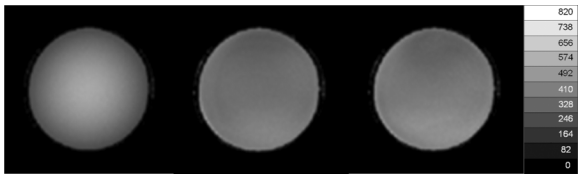

Fig. 4. T_1 maps of the phantom at the middle slice without B_1 correction (left), corrected using the B_1 map acquired at the same position (middle), and corrected using the B_1 map acquired at a position 1.7 cm apart.

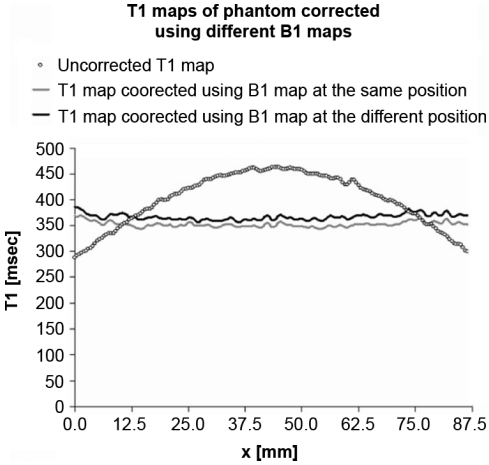

Fig. 5. Profile of the T_1 map along a diametral line at the middle slice without B_1 correction, corrected using the B_1 map acquired at the same position and corrected using the B_1 map acquired at a position 1.7 cm apart.

In order to estimate the T_1 variation along the direction of the displacement (left–right direction in Fig. 4) due to the asymmetry of the displaced B_1 map, an intensity profile was constructed at the middle slice for T_1^{nc}, T_1^{ref}, and T_1^{tem}.

Both T_1^{ref} and T_1^{tem} exhibited small changes along the direction of the displacement. Their respective mean values were 353 ms and 367 ms (4% difference) with standard deviations of 5.2 ms and 6.1 ms. (variability of 1.5% and 1.7%, respectively). On the other hand, the uncorrected T_1 map had a mean value of 400 ms with a standard deviation of 53 ms. (variability of 13.3%), exhibiting a profile according to the B_1 inhomogeneity (see Fig. 5).

C. Evaluation of the Affine Registration in T_1w Images

In order to evaluate the performance of the affine registration algorithm, the two subjects with the smallest (Subject I) and largest (Subject II) head volumes were selected and aligned.

Fig. 6 shows the T_1w images of those heads at a middle slice for subject I (a), subject II (b), subject II after registration (c), difference before (d) and after (e) registration. The quality of the alignment is evaluated computing the number of pixels not overlapped before and after registration. Fig. 7 shows the fraction of pixels in the head compared to the FOV of each slice throughout the central part of the head. The fraction of pixels of Subject I not overlapped with those of Subject I is noticeably reduced at each slice after affine registration.

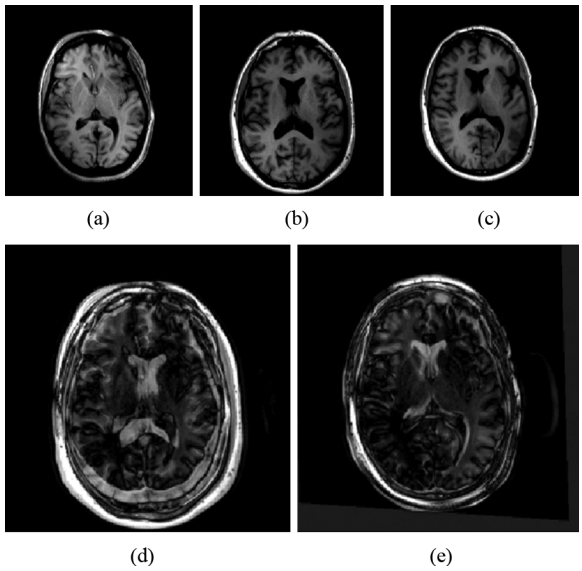

Fig. 6. T_1w images at a middle slice for: (a) Subject I (smallest head volume); (b) Subject II (largest head volume); (c) Subject II aligned to Subject I; (d) difference before affine registration; (e) difference after affine registration.

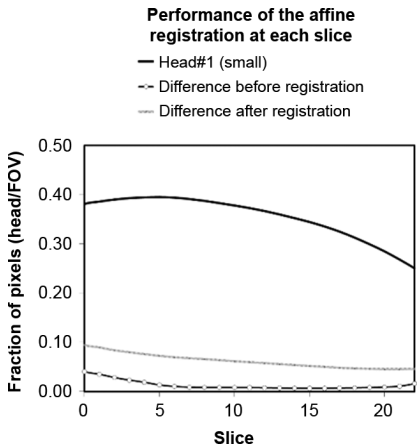

Fig. 7. Fraction of pixels in the head at each slice throughout the central part of the head.

D. In Vivo T_1 Mapping

Nineteen healthy volunteers were considered for this study and scanned in a 3T Philips MRI scanner in order to investigate the improvement of the T_1 maps after misalignment correction and B_1 correction.

Brains were extracted from those T_1 maps and intensity histograms were computed for fully corrected, partially corrected and noncorrected maps. None of the maps without B_1 correction exhibited the typical two-peak histogram corresponding to WM and GM tissues. Instead, two-peak histograms were observed in seventeen maps with B_1 correction and in every map with both corrections. Most subjects had their two T_1w images almost aligned. Therefore, no significant change could be observed in the histograms when the misalignment correction was included [Fig. 8(a)–(d)]. However, T_1w images of Subjects 8 and 15 were slightly misaligned resulting in distorted T_1 maps

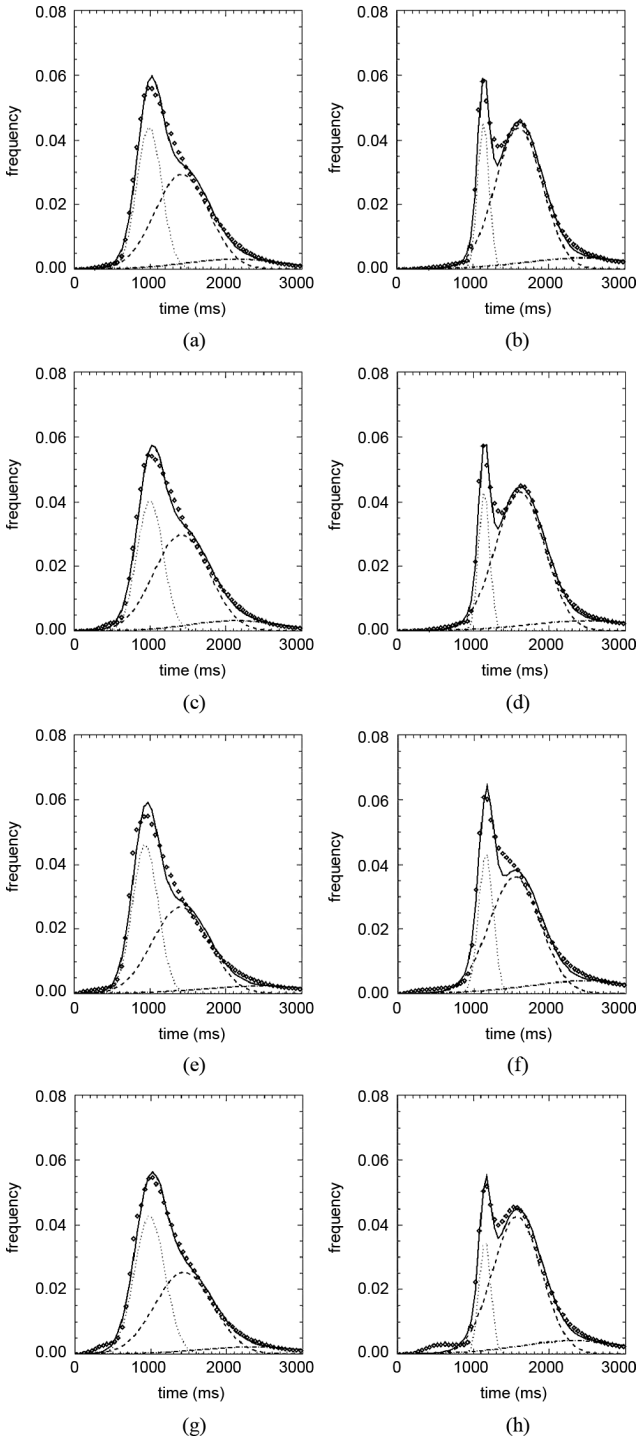

Fig. 8. Examples of B_1 corrected T_1 map histograms. Upper panel: Volunteer #14. Lower panel: Volunteer #15. For each panel: no B_1 correction (a), (e), B_1 correction (b), (f), motion correction (c), (g) and B_1 correction after motion correction (d), (h). Images were originally aligned. In each plot, points correspond to measured values, dotted lines to each fitted Gaussian curve and solid line to 3-Gaussian curve.

whose histograms did not exhibit two peaks when only B_1 correction is preformed [Fig. 8(f)]. In those cases, effects of misalignment and B_1 inhomogeneity were comparable. Distorted T_1 maps due to misalignment in Subject #15 can be seen in Fig. 8(e) and (f). It can also be observed that B_1 corrected maps

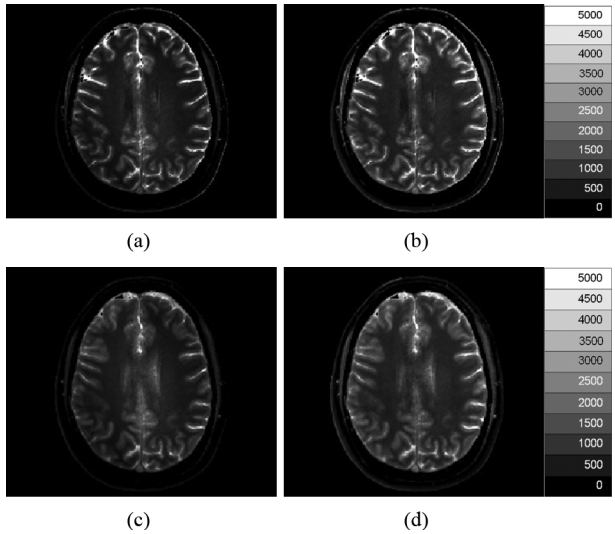

Fig. 9. T_1 maps (in ms) for Sub. #15 with the same window/level settings with (a) no correction, (b) B_1 correction, (c) misalignment correction, (d) both B_1 and misalignment correction.

[Fig. 8(f) and (h)] exhibit better discriminations of tissues than their noncorrected counterparts [Fig. 8(e) and (g)].

Fig. 9 shows T_1 maps at a middle slice for Subject #15 with and without B_1 and misalignment corrections. T_1 maps with B_1 correction [Fig. 9(b) and (d)] exhibit WM and GM regions with higher intensities (T_1 values) when compared to those without B_1 correction [Fig. 9(a) and (c)]. That is in agreement with the predicted shift discussed in Section II-C.

White and gray matter peaks along with their dispersion σ for all volunteers with and without misalignment and B_1 correction were computed from the three Gaussian fitting. The goodness of fit for the histograms was characterized by a Chi-square parameter that ranged between 0.0001 and 0.0005 among all curves. White matter and gray matter peaks were 1107 ± 80 ms and 1558 ± 88 ms, respectively, averaged over the 19 subjects. These results are in agreement with reported findings at 3.0T: WM from 1000 to 1100 ms and different GM tissues between 1200 and 1700 ms [32] using their Driven Equilibrium Single Pulse Observation of T_1 with High-Speed Incorporation of RF Field Inhomogeneities method (DESPOT1-HIFI).

Reduced spatial inhomogeneity of T_1 values within regions of the same kind of tissue after B_1 correction results in narrower WM and GM and separation of both peaks. In every subject the dispersion of WM peaks computed from the three Gaussian fitting exhibits and important reduction when B_1 correction is used, resulting in an average reduction of about 50%. Additionally, relaxation times of WM and GM peaks exhibit a noticeable shift towards higher values. In order to explain that shift B_1 maps were studied. It was observed that the mean value ranged between 0.85 and 0.96 (average $\pm$ stdev $= 0.89 \pm 0.03$) with a dispersion ranging between 0.36 and 0.427 (average $\pm$ stdev $= 0.31 \pm 0.04$). According to what it was previously discussed in Section II-C, it is expected that $\langle T_1 \rangle$ is shifted towards high relaxation times if $\langle B_1 \rangle < 1$.

TABLE II
PERCENTAGE OF VOXELS IN A GIVEN CORRECTED T_1 MAP WHOSE RELATIVE DIFFERENCE WITH RESPECT TO T_1^{ref} WAS LESS THAN 10% COMPUTED FOR ALL 10 SUBJECTS IN THE LEARNING SET FOR T_1^{opt}, T_1^{tem} AND T_1^{N3}, T_1^{nc}

Subj. #	T_1^{opt}-T_1^{ref}	T_1^{tem}-T_1^{ref}	T_1^{N3}-T_1^{ref}	T_1^{nc}-T_1^{ref}
1	63.2	63.2	48.3	37.7
2	76.3	76.3	49.7	22.2
3	51.3	35.4	59.2	36.2
4	80.4	80.4	8.1	26.9
5	81.6	81.6	16.5	25.9
6	76.5	76.5	55.6	28.1
8	72.1	72.1	41.5	33.9
15	83.4	76.2	15.6	24.8
16	73.9	73.9	26.1	27.9
19	92.6	59.7	30.9	27.7
Average	**75.1**	**69.5**	**35.2**	**29.1**

E. Template-Based B_1 Correction

In order to investigate whether or not T_1 maps can be accurately corrected using a B_1 map from another subject, T_1 maps were computed from rigidly registered T_1w images including inhomogeneity correction using transformed B_1 maps from the other subjects, and compared to T_1^{ref}. The percentage of voxels in a given corrected T_1 map whose relative difference with respect to T_1^{ref} was less than 10% was used as a quality factor for the correction. Table II shows that factor computed for all subjects in the learning set (Subjects #1, #2, #3, #4, #5, #6, #8, #15, #16, and #19) for T_1^{nc}, $T_1^{\mathrm{tem}}T_1^{N3}$. In average, that percentage increased from 29.1% for T_1^{nc} up to 75.1% for T_1^{tem}, while T_1^{N3} showed similar performance as the noncorrected map (35.2%).

The best correction could not be predicted using only one feature. Instead, a total of six features were computed in the learning set and compared to their counterparts in the reference set. Corrected T_1 maps with unimodal histograms were excluded from this analysis. In order to determine the best way in which those feature have to be combined to maximize the performance of the method, the optimum set of weighting factors was computed over the learning set. It was found that those weighting factors were $w_1 = 2/14$; $w_2 = 2/14$; $w_3 = 1/14$; $w_4 = 1/14$; $w_5 = 4/14$ and $w_6 = 4/14$, for feature F_1 to F_6, respectively. The weight scheme depicted correctly the best correction (i.e., $T_1^{\mathrm{tem}} = T_1^{\mathrm{opt}}$) in seven out of ten subjects (70%). The other subjects are discussed below.

For Subject #3 it is worth to mention that this subject's B_1 map has the highest mean value (0.962) when compared to the other 18 cases (average $= 0.894$). The three B_1 maps with closest mean values were those corresponding to subjects #1 (0.951), #18 (0.934), and #8 (0.926). The percentage of voxels in those corrected T_1 maps that had a difference less than 10% with respect to T_1^{ref} were 51.3%, 43.2%, and 35.4% for those three corrections. Note that the percentage for T_1^{nc} was 36.2%. All the other corrections had percentages below that threshold, which means that almost no correction performed better than T_1^{nc}. An explanation for that comes from the relation between T_1 and B_1 shown in Fig. 1. If the average value of the B_1 map used for the correction is very different from the real B_1 map, higher shifts in the T_1 maps are expected with respect to T_1^{ref}. Therefore, even though almost all histograms were bimodal and consequently more homogeneous, WM and GM peaks were shifted towards higher relaxation times. That drastically increased the percentage used to characterize the quality of the correction. However, the method detected for Subject #3 the third best correction (using the B_1 map from Subject #8), which was ranked as 61% in the ranking list L_1 (see Section II-F).

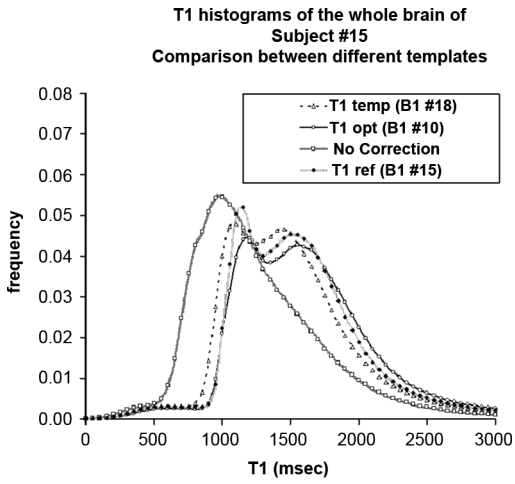

(a)

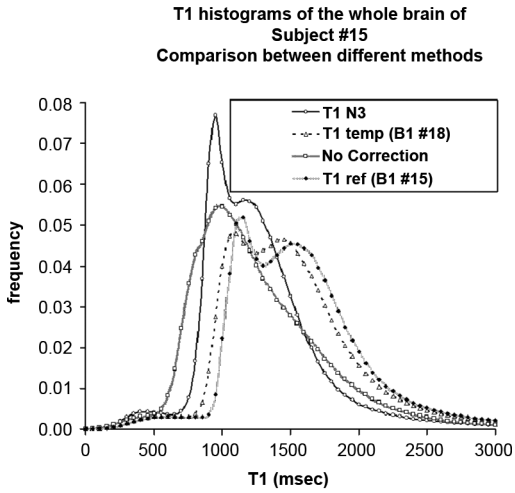

(b)

Fig. 10. T_1 histograms of the whole brain of Subject #15 corrected using different method: (a) B_1 map from the same subject ($T_{1\,(15)}^{\mathrm{ref}}$), B_1 map from Subject #18, which is the best map detected by the method ($T_{1\,(15)}^{\mathrm{tem=18}}$), B_1 map from Subject #10, which is the best available map ($T_{1\,(15)}^{\mathrm{opt=10}}$), and no B_1 correction ($T_{1\,(15)}^{nc}$); (b) T_1 map computed from T_1w images corrected using the N3 method (T_1^{N3}), T_1^{ref}, T_1^{nc}, and $T_{1\,(15)}^{\mathrm{tem=18}}$.

For Subject #15 the method also detected the third best correction (from Subject #18). However, the percentage of voxels with a difference less than 10% with respect to T_1^{ref} was high: 76.2% compared to 24.8% for the uncorrected map. For the best (from Subject #10) and worst (from Subject #7) corrections available, those percentages were 83.4% and 43.8%, respectively. Therefore, the method detected a correction that ranked as 82% in the ranking list L_1. Fig. 10(a) and (b) shows the histograms for T_1^{nc}, T_1^{ref}, T_1^{tem}, and T_1^{opt}. Small differences can be seen between histograms of T_1^{ref}, T_1^{tem}, T_1^{opt}, which are shifted with respect to those of T_1^{nc} and T_1^{N3}.

Fig. 11 shows three B_1 maps used to perform the inhomogeneity correction in this subject: a) acquired in the same Sub-

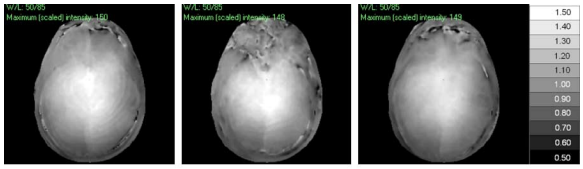

(a) (b) (c)

Fig. 11. B_1 maps used to correct T_1 maps of Subject #15 displayed with the same window/level settings, showing the position of the profile line: (a) B_1 map of Subject #15; (b) B_1 map of Subject #18 (best correction detected by our method) after proper affine registration; (c) B_1 map of Subject #10 (best non-subject-specific correction available) after proper affine registration.

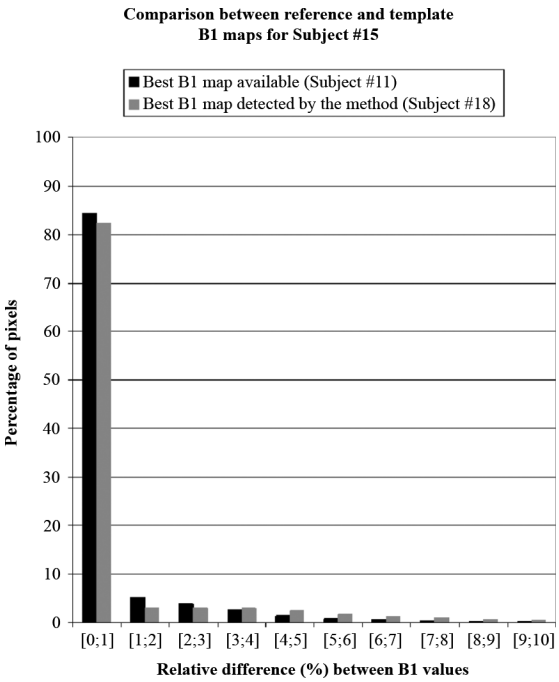

Fig. 12. Percentage of pixels in those template B_1 maps having a given relative difference with respect to the reference B_1 map.

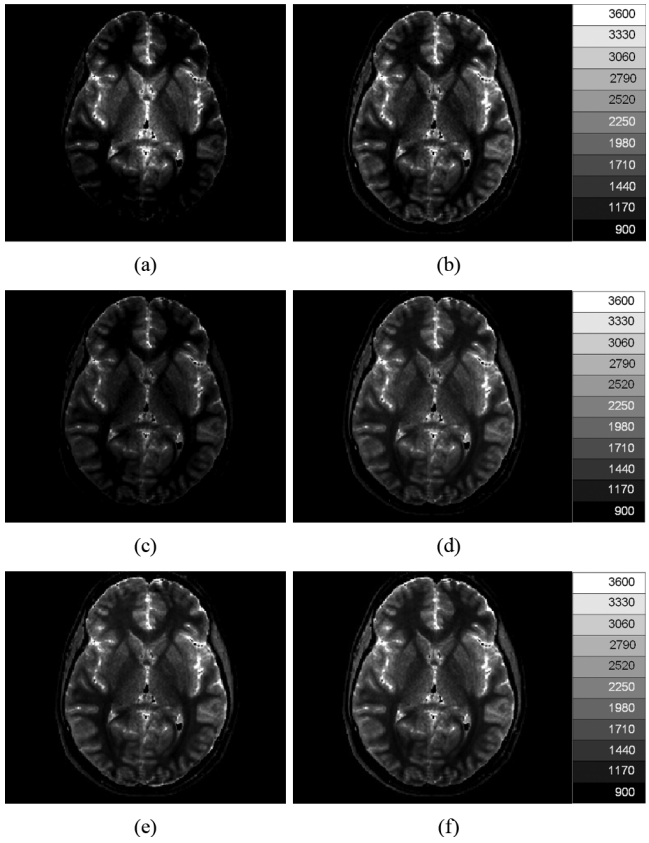

Fig. 13. T_1 maps (in ms) for Subject #15 computed using different B_1 corrections displayed with the same window/level settings: (a) no B_1 correction, T_1^{nc}; (b) reference T_1 map, T_1^{ref}; (c) N3 method, T_1^{N3}; (d) corrected using the B_1 map from the same Subject #15 but under a linear approximation, T_1^{lin}; (e) corrected using the B_1 map from Subject #18, $T_1^{(18)}$ (best correction detected by our method, T_1^{tem}); (f) corrected using the B_1 map from Subject #10, $T_1^{(10)}$ (best nonsubject-specific correction available, T_1^{opt}).

ject #15; b) acquired in Subject #18 (best correction detected by our method); c) acquired in Subject #10 (best correction available for this subject).

Fig. 12 shows the percentage of pixels in the template B_1 maps for Subject #15 for relative differences with respect to the reference B_1 map less than 10%. Particularly, for the best available B_1 map, 93.3% of the pixels have a difference less than 3%. For the B_1 map detected by the method, that percentage is 88.2%.

T_1 maps for Subject #15 are displayed in Fig. 13 under different corrections: a) no B_1 correction; b) reference T_1 map ($T_{1\,15}^{15}$); c) N3 method ($T_{1\,15}^{N3}$); d) corrected using the B_1 map from the same Subject #15 but under a linear approximation ($T_{1\,15}^{\mathrm{lin}}$) shown in Fig. 1; e) corrected using the B_1 map from Subject #18 ($T_{1\,15}^{\mathrm{tem}=18}$); and f) corrected using the B_1 map from Subject #10 ($T_{1\,15}^{\mathrm{opt}=10}$). No relevant differences can be observed between those maps corrected with the B_1 map of the same subject, with and without the linear approximation [Fig. 13(b) and (d)]. T_1 map corrected with the N3 method [Fig. 13(c)] shows lower intensities as in the noncorrected map [Fig. 13(a)], but without inhomogeneity throughout voxels of the same tissues. T_1 maps corrected with the B_1 map detect by our method [Fig. 13(e)] and the best correction available [Fig. 13(f)] do not differ significantly. The corresponding histograms are shown in Fig. 10(a) and (b). It can also be observed that $T_{1\,15}^{15}$, $T_{1\,15}^{18}$ and $T_{1\,15}^{10}$ do not exhibit significant differences. $T_{1\,15}^{N3}$ has a lower mean value similar to that of $T_{1\,15}^{nc}$.

For Subject #19 the method detected a correction (T_1^{tem}) that ranked as 41% in the L_1 list. However, given that for this subject the best correction (T_1^{opt}) was comparable to T_1^{ref} (92.6% of the voxels had a difference less than 10%), that percentage was 59.7% for T_1^{tem}, which was still higher than the 27.7% corresponding to T_1^{nc}.

It is expected that the bigger the library size is, the more accurate the correction will be. However, the study does not contain sufficient number of cases to perform a reliable convergence analysis. Instead, we designed a simple experiment to estimate the effect of the library size on the accuracy of the correction. For each subject in the learning set, the best template was removed from the library. Therefore, the method found the following best template. The position in the ranking list was obtained and compared to the best template. For the seven cases where the method detected the best template the average position in the ranking list dropped to 87%. The complete list is found in Table III.

TABLE III
POSITIONS IN THE RANKING LIST OF THE TEMPLATE DETECTED BY THE METHOD WHEN THE BEST TEMPLATE IS INCLUDED (A) AND WHEN IT IS NOT CONSIDERED (B)

Subj. #	Ranking with best template (a)	Ranking without the best template (b)
1	100	87
2	100	84
3	61	61
4	100	91
5	100	70
6	100	90
8	100	98
15	82	82
16	100	85
19	41	41

It is important to mention that no correlation was found between the age, the head size and the sex of the subject under study and the subject of the best available template. Particularly, the standard deviation of ages was 11.3 years, while that of the age difference between both subjects was 9.8 years. For the head sizes, those values were $502\ \mathrm{cm}^3$ and $468\ \mathrm{cm}^3$. Regarding the sex, only 60% of the best available templates corresponded to same sex individuals. Finally, Fig. 14 shows all the nineteen B_1 maps at the middle slice used for this study (same w/l settings), after being mapped to the same space. Fig. 15 shows all the B_1 maps in the learning set along with the best template, exhibiting similarities between them.

F. Comparison to Deoni's DESPOT1-HI-FI Method

Alternatively to Treier's method, Deoni's DESPOT1-HI-FI technique combines the usual multiangle SPGR data with at least one inversion-prepared SPGR data in order to obtain an unique solution for the T_1 map, the factor proportional to the longitudinal magnetization and the spatial variation of the radio-frequency field by least square minimization, which requires 6:40 min for a T_1 map ($128 \times 128 \times 160$ matrix) [32]. That acquisition time is much shorter than multiple inversion time IR-SPGR (14:43 min) and the acceleration Lock-Locker approach (26 min). Instead, out scanning time using a $480 \times 480 \times 48$ matrix for low- and high-flip $-T_1w$ images, and a $240 \times 240 \times 24$ matrix for the low and high $T_R - T_1w$ images) is 7:30 min total.

For comparison purposes we also performed acquisitions using Deoni's technique. The SPGR signal equation in its linear form is given by (2). Both T_1 and a factor proportional to the longitudinal magnetization can be computed from the slope and the intercept of this relation. We used an inversion recovery SPGR approach called DESPOT1-HI-FI involving application of a 180° inversion pulse, an inversion time (TI) delay and a train of low angle RF pulses, separated by a T_R, which sample successive k-space lines. If the center of k-space is acquired immediately following each 180° pulse, the IR-SPGR signal can be approximated as

$$S_{\mathrm{IR-SPGR}} = \rho\left[1-(1-\cos k180^\circ)\,e^{-TI/T_1}+e^{-TR/T_1}\right]\sin k\alpha_p \quad (17)$$

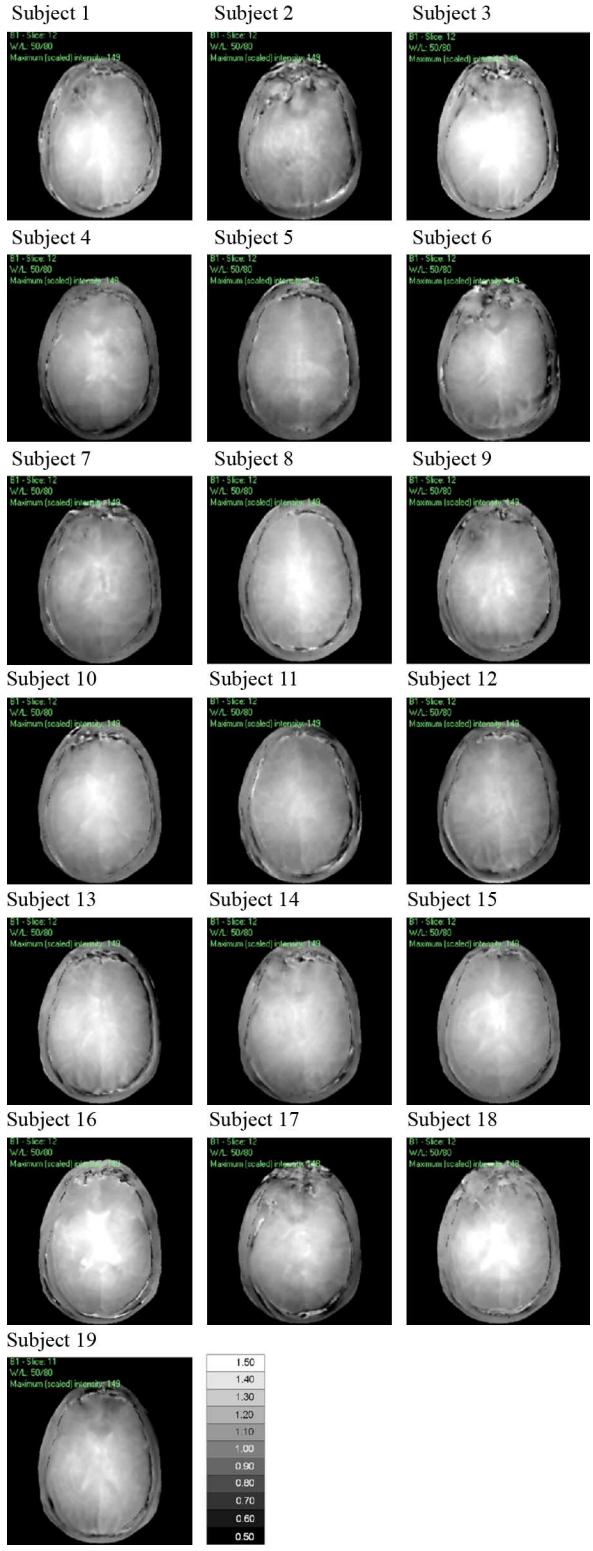

Fig. 14. All B_1 maps at a middle slice used in this study, with the same window/level settings, after being mapped to the same space.

where T_R is the time between 180° pulses and k denotes the spatially varying α_p profile ($\alpha_p = k\alpha_p$). A unique solution for T_1, ρ, and k can then be calculated using least-squares minimization of (3) and (17) [38]. The k parameter map represents the scaling correction of the flip angles, i.e., B_1 error.

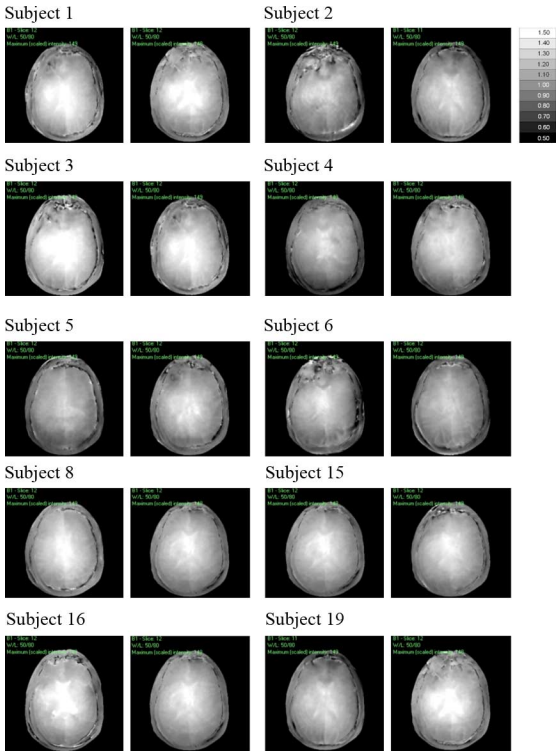

Fig. 15. B_1 maps of all subjects in the learning set along with the B_1 map of the best template, displayed at the middle slice with the same window/level settings.

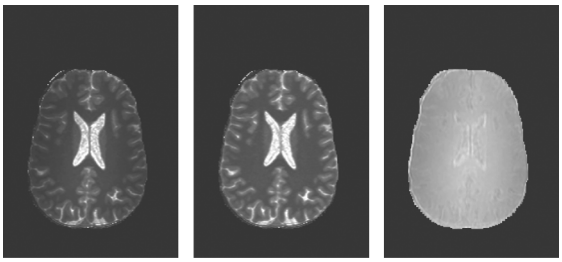

Fig. 16. T_1 map without B_1 correction (a), with B_1 correction (b) and B_1 map (c) of a healthy volunteer using DESPOT-HI-FI method.

TABLE IV
MEAN VALUES AND DEVIATION OF WM AND GM REGIONS IN T_1 MAP OF A HEALTHY VOLUNTEER USING DESPOT-HI-FI WITH AND WITHOUT B_1 CORRECTION

	<WM> ; σ_{WM} (ms)	<GM> ; σ_{GM} (ms)
W/O B_1 correction	660 ; 173	1146 ; 323
W B_1 correction	1000 ; 169	1419 ; 275

In order to compare our methodology, based on Treier's method, to the Deoni's DESPOT1-HI-FI mapping with B_1 correction, we scanned an additional healthy volunteer using that technique. The acquisition time was 19 min for a $256\times256\times276$ matrix. B_1 maps acquired using Deoni's and Treier's technique had similar overall characteristics (see Fig. 16). Furthermore, mean WM and GM in the corrected and uncorrected maps are in the range of those found in our work (see Table IV).

IV. DISCUSSION

Accurate estimation of T_1 relaxation time from high magnetic field MRI using a dual flip angle method may require correction of not only the transmitted flip angle inhomogeneity but also any possible image misalignment. In order to investigate this hypothesis we addressed both corrections by acquiring the B_1 map using a dual T_R strategy and a rigid registration algorithm.

The B_1 correction module was evaluated using a spherical phantom resulting in a narrower T_1 intensity histogram whose mean value is in agreement to that from an inversion recovery technique. It was also observed that retrospective methods like the N3 method that preserve the mean value of the T_1 map do not show the observed shift in relaxation times between T_1^{nc} and T_1^{ref}. Although methods that preserve the mean T_1 value remove the inhomogeneity producing bimodal histograms, those T_1 values are shifted with respect to those in maps corrected with a B_1 map. Those corrections may not be suitable for quantitative analyses.

T_1 maps were analyzed in nineteen normal volunteers. Prior to B_1 correction, histograms of whole brain did not exhibit a bimodal peak (WM and GM). On the other hand, all corrected histograms showed two separated peaks whose T_1 values are in agreement with previously reported data. However, slightly misaligned T_1w images used to compute T_1 maps resulted in inaccurate T_1 map in two subjects. In those cases, image misalignment and flip angle inhomogeneity produced comparable effects on that map, whose histogram did not exhibit two peaks when only B_1 correction was performed.

In order to obviate the need for obtaining a B_1 map each and every time a patient is scanned, a template B_1 map may be used instead. Therefore, each T_1 map was recomputed using the B_1 maps from the other subjects. For that purpose, twelve-parameter affine registration using mutual information metric with linear interpolation was applied to each pair of high-flip-angle images. The computed transformation was applied to the B_1 map in order to match the geometry of the subject under study. Although most corrections reduced the inhomogeneity, the performance depends on the B_1 map used. Therefore, in order to automatically detect the best B_1 map available, a set of features were computed and included with an optimum set of weighting factors in the minimization of a metric function. The set of features used allowed the detection of the best available B_1 map in most cases. In the others, T_1 maps comparable to the reference one are obtained.

Although results are promising and have the potential for clinical applications, the methodology has some limitations. First, acquired B_1 maps exhibit different mean values. Therefore, if all B_1 maps in the library significantly differ from the proper (even unknown) B_1 map, a shift in the corrected T_1 values would be expected. Therefore, even though the method may detect the best available B_1 map, it may not produce a T_1 map that is accurate enough. In order to avoid that, a wide range of B_1 maps with different characteristics should be included in that library. Even though that would increase the computational time to detect the best correction, we still have a reduced acquisition time.

Secondly, this methodology has the potential to improve the cancer detection by means of more accurate T_1 maps. In order to investigate whether or not the template B_1 correction of T_1

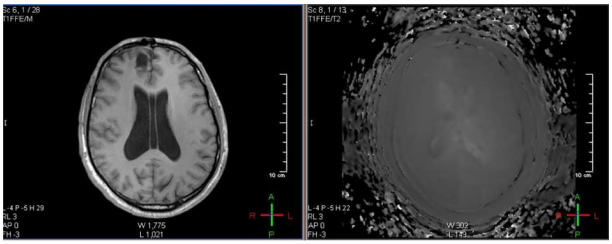

(a) (b)

Fig. 17. T_1 weighted image (a) and B_1 map (b) of a patient with a tumor in the frontal region of the brain and ventricle enlargement.

maps of a patient with a brain tumor could be applied using a library containing B_1 maps of normal subjects, the T_1 weighted images and B_1 map of a patient with a tumor in the frontal region were studied. Fig. 17 shows a B_1 map (b) associated with obvious pathology on the correlated T_1 weighted image (a). While there is significant deviation from normal brain in terms of the image contrast in the enlarged ventricles as well as frontal cortex, the corresponding B_1 map is remarkably homogeneous. This is due to the predominant mechanism of RF inhomogeneity being due to the air water susceptibility interface as the RF wave traverses the different media. Since most pathology will still consist of relatively homogeneous proton density the B_1 map is quite similar to other normal volunteer B_1 maps.

Therefore, in order for the methodology to be applied to patients with brain tumor, it should include a tumor segmentation module to compute the features only outside the tumor. While we would expect the template method to yield improved results on a clinical population, this work is currently being evaluated prior to implementation. Furthermore, the accuracy of the B_1 mapping process itself is limited if there is significant deviation from uniform proton density so correction with an inaccurate but patient specific B_1 map will also decrease the accuracy of the calculated T_1 values.

V. Conclusion

The results presented in this work show that correction of both image misalignment and transmitted flip angle inhomogeneity markedly improve the accuracy of T_1 maps obtained by means of a dual flip angle method at high fields. It was observed that the nonlinear relation between the B_1 correction factors at every voxel and the corrected T_1 value produce a shift in the mean value of the reference T_1 map when compared to the uncorrected map. That may suggest that methods that preserve that mean value could lead to inaccurate T_1 estimations regardless their ability to maximize the homogeneity within each kind of tissue. Additionally, since in the clinical setting it is beneficial to minimize scanning time and it would be desirable that B_1 corrections may be made from a template, obviating the need for obtaining a B_1 map each and every time a patient is scanned. B_1 inhomogeneity in T_1 maps computed from registered images were also compensated using B_1 maps acquired from other subjects, after being aligned using an affine registration algorithm.

When B_1 maps from other subjects are properly aligned, many corrected T_1 maps are comparable to the reference T_1 map and a considerable number of other maps exhibit a relevant improvement when compared to the noncorrected ones. An automatic method to characterize the quality of the correction and detect the B_1 map that best performs for a given subject was designed and evaluated. Even though a larger study is needed to corroborate the efficiency of the method, these results are very promising and have the potential for clinical application.

Acknowledgment

The authors would like to acknowledge Image Processing Specialist F. Thomas at Clinical Image Processing Services (CIPS, DR&IS, National Institutes of Health, Bethesda, MD), for collaborating in the image processing.

References

[1] P. L. Choyke, A. J. Dwyer, and M. V. Knopp, "Functional tumor imaging with dynamic contrast-enchanced magnetic resonance imaging," *J. Magn. Reson. Imag.*, vol. 17, pp. 509–520, 2003.

[2] A. R. Padhani and J. E. Husband, "Dynamic contrast-enhanced MRI studies in oncology, with an emphasis on quantification, validation and human studies," *Clin. Radiol.*, vol. 56, pp. 607–620, 2001.

[3] P. S. Tofts *et al.*, "Estimating kinetic parameters from dynamic contrast-enhanced t1-weighted MRI of a diffusible tracer: Strandarized quantities and symbols," *J. Magn. Reson. Imag.*, vol. 10, no. 3, pp. 223–232, 1999.

[4] H.-L. M. Cheng and G. A. Wright, "Rapid high-resolution T_1 mapping by variable flip angles: Accurate and precise measurement in the presence of radiofrequency field inhomogeneity," *Magn. Reson. Med.*, vol. 55, pp. 566–574, 2006.

[5] S. C. L. Deoni, T. M. Peters, and B. K. Rutt, "Determination of optimal angles for variable nutation proton magnetic spin-lattice, T_1, spin-spin, T_2, relaxation times measurements," *Magn. Reson. Med.*, vol. 51, pp. 194–199, 2004.

[6] H. Wang, S. Riederer, and J. Lee, "Optimizing the precision in T_1 relaxation estimation using limited flip angles," *Magn. Reson.Med.*, vol. 5, pp. 399–416, 1987.

[7] J. G. Sled and G. B. Pike, "Understanding intensity non-uniformity in MRI," *Proc. MICCAI 1998*, pp. 614–622, 1998, Lecture Notes on Computer Science.

[8] W. A. Edelstein, G. H. Glover, C. J. Hardy, and R. W. Redington, "The intrinsic signal-to-Noise ratio in NMR imaging," *Magn. Reson. Med.*, vol. 3, pp. 604–618, 1986.

[9] J. M. Jin, J. Chen, W. C. Chew, H. Gan, R. L. Magin, and P. J. Dimbylow, "Computation of electromagnetic fields for high-frequency magnetic resonance imaging applications," *Phys. Med. Biol.*, vol. 41, pp. 2719–2738, 1996.

[10] O. Dietrich, M. F. Reiser, and S. O. Schoenberg, "Artifacts in 3-Tesla MRI: Physical background and reduction strategies," *Eur. J. Radiol.*, vol. 65, pp. 29–35, 2008.

[11] B. Belaroussi, J. Mille, S. Carme, Y. M. Zhu, and H. Benoit-Catin, "Intensity non-uniformity correction in MRI: Existing methods and their validation," *Med. Image Anal.*, vol. 10, pp. 234–246, 2006.

[12] U. Vovk, F. Pernus, and B. Likar, "A review of methods for correction of intensity inhomogeneity in MRI," *IEEE Trans. Med. Imag.*, vol. 26, no. 3, pp. 405–421, Mar. 2007.

[13] Z. Hou, "A review on MR image intensity inhomogeneity correction," *Int. J. Biomed. Imag.*, vol. 2006, pp. 1–11, 2006.

[14] B. H. Brinkmann, A. Manduca, and R. A. Robb, "Optimized homomorphic unsharp masking for MR grayscale inhomogeneity correction," *IEEE Trans. Med. Imag.*, vol. 17, no. 2, pp. 161–171, Apr. 1998.

[15] B. M. Dawant, A. P. Zijdenbos, and R. A. Margolin, "Correction of intensity variations in MR images for coumpted-aided tissue classification," *IEEE Trans. Med. Imag.*, vol. 12, no. 4, pp. 770–781, Dec. 1993.

[16] C. Han, T. S. Hatsukami, and C. Yuan, "A multi-scale methods for automatic correction of intensity non-uniformity in MR images," *J. Magn. Reson. Imag.*, vol. 13, pp. 428–436, 2001.

[17] A. W.-C. Liew and H. Yan, "An addaptive spatial fuzzy clustering algorithm for 3-D MR image segmentation," *IEEE Trans. Med. Imag.*, vol. 22, no. 9, pp. 1063–1075, Sep. 2003.

[18] B. Likar, B. A. Maintz, and M. A. Viergever, "Retrospective shading correction based on entropy minimization," *J. Microscopy*, vol. 197, pp. 285–295, 2000.

[19] B. Likar, M. A. Viergever, and F. Pernus, "Retrospective correction of MR intensity inhomogeneity by information minimization," *IEEE Trans. Med. Imag.*, vol. 20, no. 12, pp. 1398–1410, Dec. 2001.

[20] F. Lin, Y. Chen, J. W. Belliveau, and L. L. Wald, "A wavelet-based approximation of surface coil sensitivity profiles for correction of image intensity inhomogeneity and parallel image reconstruction," *Hum. Brain Mapp.*, vol. 19, pp. 96–111, 2003.

[21] J. Luo, Y. Zhu, P. Clarysee, and I. Magnin, "Correction of bias field in MR images using singulatiry function analysis," *IEEE Trans. Med. Imag.*, vol. 24, no. 8, pp. 1067–1085, Aug. 2005.

[22] J. F. Mangin, "Entropy minimization for automatic correction of intensity nonuniformity," presented at the IEEE Workshop on Mathematical Methods in Biomedical Image Analysis, Hilton Head Island, SC, 2000.

[23] J. L. Marroquin, B. C. Bemuri, S. Botello, F. Calderon, and A. Fernandez-Bouzas, "An accurate and efficient bayesian method for automatic segmentation of brain MRI," *IEEE Trans. Med. Imag.*, vol. 21, no. 8, pp. 934–945, Aug. 2002.

[24] C. R. Meyer, P. H. Bland, and J. Pipe, "Retrospective correction of intensity inhomogeneities in MRI," *IEEE Trans. Med. Imag.*, vol. 14, no. 1, pp. 36–41, Mar. 1995.

[25] J. G. Sled and A. P. Zijdenbos, "A nonparametric method for automatic correction of intensity nonuniformity in MRI data," *IEEE Trans. Med. Imag.*, vol. 17, no. 1, pp. 87–97, Feb. 1998.

[26] C. Studholme, V. Cardenas, E. Song, F. Ezekiel, A. Maudsley, and M. Weiner, "Accurate template-based correction of brain MRI intensity distortion with application to dementia and aging," *IEEE Trans. Med. Imag.*, vol. 23, no. 1, pp. 99–110, Jan. 2004.

[27] Y. Zhang, M. Brady, and S. Smith, "Segmentation of brain MR images through a hidden Markov random field model and the expectation-maximization algorithm," *IEEE Trans. Med. Imag.*, vol. 20, no. 1, pp. 45–57, Jan. 2001.

[28] Y. Ishimori, K. Yamada, H. Kimura, Y. Fujiwara, I. Yamaguchi, M. Monma, and H. Uematsu, "Correction of inhomogeneous RF field using multiple SPGR signals for high-field spin-echo MRI," *Magn. Reson. Med. Sci.*, vol. 6, pp. 67–73, 2007.

[29] H. Mihara, M. Sekino, N. Iriguchi, and S. Ueno, "A method for an accurate T_1 relaxation-time measurement compensating B_1 field inhomogeneity in magnetic-resonance imaging," presented at the 49th Annu. Conf. Magn. Magn. Mater., Jacksonville, FL, 2005.

[30] R. TrSeier, A. Steingoetter, M. Fried, W. Schwizer, and P. Boesiger, "Optimized and combined T_1 and B_1 mapping technique for fast accurate T_1 quantification in constrast-enhanced abdominal MRI," *Magn. Reson. Med.*, vol. 57, pp. 568–576, 2007.

[31] V. Yarnykh, "Actual flip-angle imaging in the pulsed steady state: A method for rapid 3D mapping of the transmitted radiofrequency field," *Magn. Reson. Med.*, vol. 57, pp. 192–200, 2007.

[32] S. C. L. Deoni, "High-resolution T_1 mapping of the brain at 3T with driven equilibrium single pulse observation with T_1 high-speed incorporation of RF field inhomogeneities (DESPOT1-HIFI)," *J. Magn. Reson. Imag.*, vol. 26, pp. 1106–1111, 2007.

[33] M. A. Castro, J. Yao, C. Lee, Y. Pang, E. Baker, J. Butman, and D. Thomasson, "T_1 mapping with B_1 field and motion correction in brain MRI images: Application to brain DCE-MRI," presented at the MICCAI 2008-Workshop Anal. Functional Med. Images, New York, 2008.

[34] S. Smith, "Fast robust automated brain extraction," *Hum. Brain Mapp.*, vol. 17, pp. 143–155, 2002.

[35] S. Ruan, C. Jaggi, J. Xue, J. Fadili, and D. Blovet, "Brain tissue classification of magnetic resonance images using partial volume modeling," *IEEE Trans. Med. Imag.*, vol. 19, no. 12, pp. 1179–1187, Dec. 2000.

[36] P. Viola and W. M. Wells, III, "Alignment by maximization of mutual information," *Int. J. Comput. Vis.*, vol. 24, no. 2, pp. 137–154, 1997.

[37] S. C. L. Deoni, B. K. Rutt, and T. M. Peters, "Rapid combined T_1 and T_2 mapping using gradient recalled acquisition in the steady state," *Magn. Reson. Med.*, vol. 49, pp. 515–526, 2003.

[38] R. Stolleberg and P. Wach, "Imaging of the active B_1 field in vivo," *Magn. Reson. Med.*, vol. 35, pp. 246–251, 1996.